Nanoscale Advances

ROYAL SOCIETY OF CHEMISTRY

PAPER

View Article Online
View Journal | View Issue

Cite this: *Nanoscale Adv.*, 2021, **3**, 1758

A reconfigurable hyperbolic metamaterial perfect absorber†

Jitendra K. Behera,‡ Kuan Liu, Meng Lian and Tun Cao ‡*

Metamaterial (MM) perfect absorbers are realised over various spectra from visible to microwave. Recently, different approaches have been explored to integrate tunability into MM absorbers. Particularly, tuning has been illustrated through electrical-, thermal-, and photo-induced changes to the permittivity of the active medium within MM absorbers. However, the intricate design, expensive nanofabrication process, and the volatile nature of the active medium limit the widespread applications of MM absorbers. Metal–dielectric stack layered hyperbolic metamaterials (HMMs) have recently attracted much attention due to their extraordinary optical properties and rather simple design. Herein, we experimentally realised a reconfigurable HMM perfect absorber based on alternating gold (Au) and $Ge_2Sb_2Te_5$ (GST225) layers for the near-infrared (N-IR) region. It shows that a red-shift of 500 nm of the absorptance peak can be obtained by changing the GST225 state from amorphous to crystalline. The nearly perfect absorptance is omnidirectional and polarisation-independent. Additionally, the absorptance peak can be reversibly switched in just five nanoseconds by re-amorphising the GST225, enabling a dynamically reconfigurable HMM absorber. Experimental data are validated numerically using the finite-difference time-domain method. The absorber fabricated using our strategy has advantages of being reconfigurable, uncomplicated, and lithography-free over conventional MM absorbers, which may open up a new path for applications in energy harvesting, photodetectors, biochemical sensing, and thermal camouflage techniques.

Received 23rd September 2020
Accepted 29th January 2021

DOI: 10.1039/d0na00787k

rsc.li/nanoscale-advances

1. Introduction

Perfect absorption achieved by photonic devices is promising for many applications such as energy harvesting, radiative cooling, thermal emitters, photodetectors, solar cells, thermal imaging, optical modulators, and colour filters.[1–19] Recently, metamaterial (MM) perfect absorbers have been demonstrated in the spectra ranging from visible to GHz.[20–28] By adjusting the resonances in the effective permittivity and permeability independently, one can match the impedance of MMs to that of free-space to obtain a high absorption. Nevertheless, some disadvantages hold back the commercial potential of MM absorbers. For example, the subwavelength-scale meta-atom needs to be fabricated using top-down lithography techniques *i.e.*, focused ion beam (FIB) milling or electron-beam lithography (EBL). Those techniques have restricted spatial resolution and are very hard to scale up to large-field patterning; moreover, since they are serial writing techniques, the fabrication throughput is low. To solve the problem, recently a few remarkable techniques have been developed to fabricate large-size MMs while having a low-cost, including nano-printing, interference lithography, *etc.*[29–31]

Alternatively, metal/dielectric stacks, so-called hyperbolic metamaterials (HMMs), have recently witnessed an exponentially increasing interest, featured by the unique property of their permittivity tensors in which the signs of diagonal components are different.[32] Specifically, photonic HMMs are uniaxial nanocomposite structures based on the permittivity tensor of the diagonal expression $[\varepsilon] = \mathrm{diag}(\varepsilon_{\parallel}, \varepsilon_{\parallel}, \varepsilon_{\perp})$. The principal elements have the opposite signs $\varepsilon_{\parallel} > 0$, $\varepsilon_{\perp} < 0$ (type-I) and $\varepsilon_{\parallel} < 0$, $\varepsilon_{\perp} > 0$ (type-II).[33] This leads to a hyperbolic-type surface of dispersion in wavevector space, defined as hyperbolic dispersion. Unlike MMs composed of subwavelength resonator arrays, HMMs exhibiting a nominally infinite density of states[34] can support EM-waves with a high propagation wavevector while not requiring periodicity in the plane normal to the incident wave and can be fabricated using conventional thin film sputtering. Therefore, they are considered appropriate for bulky-area surfaces, enabling them to be practical for applications such as super-resolution imaging,[35,36] resonant gain singularities,[37] light beam steering,[38,39] spontaneous emission enhancement,[40] super-collimation,[41] ultra-sensitive biosensors,[42,43] negative refraction,[44] and near-zero epsilon.[45] Such unique properties have enabled HMMs to be widely exploited for absorption application.[46]

School of Optoelectronic Engineering and Instrumentation Science, Dalian University of Technology, Dalian 116024, China. E-mail: caotun1806@dlut.edu.cn

† Electronic supplementary information (ESI) available. See DOI: 10.1039/d0na00787k

‡ These authors (T. C. and J. B.) contributed equally to the work.

Recently, Sreekanth *et al.* proposed a type-II (Ag/TiO_2) HMM structure for multiband perfect absorption in the near-infrared (N-IR) region.[47] A wide-angle ultra-broadband infrared (IR) absorber was demonstrated by Cui *et al.* using Ge/Au saw-toothed anisotropic MMs.[48] More recently, Lin *et al.* demonstrated a broadband perfect absorber of graphene-based HMMs.[49] Desouky *et al.* theoretically demonstrated a super absorber in the mid-infrared (M-IR) spectral range using silicon and doped silicon-based HMMs.[50] Nevertheless, the current HMM absorbers are limited to a fixed spectral region. It is because the extreme anisotropy and hyperbolic dispersion of HMMs are determined by their metal and dielectric constituents and the filling fraction, which are fixed after the fabrication.

On the other hand, different methods have been exploited to integrate tunability into HMMs, where the tunability is demonstrated through stimulus sensitive functional dielectrics, *i.e.*, conductive oxides,[51] liquid crystals,[52] gyromagnetics,[53] or semiconductors.[54] It allows for active control of HMM properties by photo-, electrical-, and thermal-induced variations to the permittivity of the active dielectric within the HMM structure. Yet, so far rare efforts have been made to obtain a reversibly tunable HMM absorber. There are, however, loads of applications where a reconfigurable light absorption is highly wanted. For example, a switchable perfect absorber can find important applications in electro-optic switches,[55] selective thermal emitters,[56] and tunable sensors.[57] Furthermore, in HMM absorbers the dielectric components are passive (*i.e.*, SiO_2 and TiO_2), which does not change the absorbed photons into electron–hole pairs. This forbids their applications for photodetectors and photovoltaic cells. These issues motivate our study, in which we look into actively reconfigurable HMM perfect absorbers over genuinely macroscopic size *via* a scalable, straightforward, and low-cost fabrication procedure.

The family of chalcogenide semiconductors of the Ge–Sb–Te (GST) phase-change material (PCM) exhibits two stable structural states: amorphous and crystalline. GST can undergo a reversible structural transition, leading to a substantial change in its optical and electrical properties. Such a unique characteristic enables them to be suitable for photonics applications, ranging from multilevel storage and displays to integrated nanophotonic systems.[58] Due to its prompt state transition, high cyclability, and outstanding thermal stability, GST is important for high-speed and switchable photonic devices.[59–61] For example, tunable negative index metamaterials,[62] rewritable metasurface lenses,[63] thermal emitters,[56] beam steering[64,65] and tunable chirality[66,67] have been explored. Recently, GST has been demonstrated as a promising candidate functional dielectric to perform as a tunable metasurface perfect absorber in the mid-infrared (M-IR) spectrum.[11] Nevertheless, this tuning strategy turns out to be unrealistic for the N-IR spectrum. It is because the fabrication of periodic nano-antenna arrays working in the N-IR region needs either FIB or EBL patterning, which is high-cost and time-consuming. The N-IR spectrum is, however, a technologically key spectrum with highly significant applications like molecular sensing and optical telecommunications.[68]

In this work, we demonstrate a tunable HMM perfect absorber based on bilayer stacks consisting of alternating gold (Au) and a prototypical PCM, $Ge_2Sb_2Te_5$ (GST225) of sub-wavelength thickness. A non-volatile ultrafast reconfigurable HMM perfect absorber is experimentally obtained by exploring the reversible amorphous-to-crystalline state change of GST225. The HMM structure maintains an omnidirectional perfect absorption for both p- and s-polarisations and shows type-II hyperbolic dispersion over the N-IR region. A numerical simulation based on the finite-difference time-domain (FDTD) method is performed to investigate the physics underlying the high absorption. Compared with the previous light absorber consisting of nanoantenna arrays fabricated by the top-down method, our HMM perfect absorber does not need lithographic patterning that results in advantages of scalability, low-cost, macroscopic scale and high throughput. For this work, the GST alloy is chosen as the functional material because not only its optical properties undergo a radical change during the amorphous–crystalline phase change, but also it is an active semiconductor that can convert the absorbed light energy into electron–hole pairs,[69] making the GST225 based HMM absorber useful for photodetectors or photovoltaic cells. Another key advantage of the reconfigurable HMM absorber is its non-volatile feature since the energy is only needed for the phase changing process and not for keeping a particular structural phase. Therefore, once the HMM absorber is transited, it will maintain its optical properties until it is transited again. This certainly enables HMM absorbers to be appealing from a green technology outlook. We propose that this large-area, omnidirectional, polarisation-insensitive and reconfigurable HMM absorber can be a promising candidate for energy harvesting, bio-chemical sensing, thermal emitters, photodetectors, and thermal camouflage techniques. The lithography-free and high throughput fabrication process may lead to absorption- and emissivity-controllable surfaces with arbitrary size.

2. Results and discussion

Fig. 1(a) schematically illustrates a reconfigurable HMM perfect absorber composed of Au–GST225 stacked layers, where a non-volatile bidirectional switching functionality can be realised *via* a reversible phase transition. The perfect absorber is a type-II HMM consisting of six periods of alternating planar films of 40 nm thick GST225 and Au. The HMM is fabricated on the fused silica (SiO_2) substrate by using physical vapour deposition (see Methods for details). A second electron microscopy (SEM) cross-section of the HMM (Fig. 1(b)) can be used to distinguish each GST225 and Au film. It confirms that no diffusion occurs during the layer deposition. The HMM absorber is experimentally measured using variable angle spectroscopic ellipsometry (VASE) over a wide spectral range of 400–2400 nm. The measured data are analysed by employing a uniaxial anisotropy model[46,70,71] to extract the effective out-of-plane ($\varepsilon_\perp$) and in-plane ($\varepsilon_\parallel$) permittivity of the HMM absorber. Particularly, the $\varepsilon_\parallel$ and $\varepsilon_\perp$ are obtained *via*[72,73]

$$\varepsilon_\parallel = f \times \varepsilon_{Au} + (1 - f) \times \varepsilon_{GST} \quad (1)$$

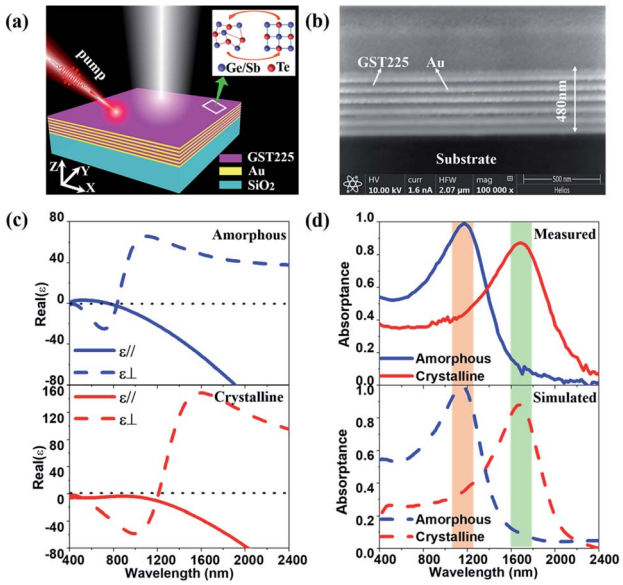

Fig. 1 (a) Scheme of the reconfigurable phase-change HMM absorber, where the structure is composed of Au–GST225 stacked layers. Both the GST225 and Au films have an identical thickness of 40 nm. The whole HMM absorber sits on a silica substrate. (b) FIB image of the cross-section of the HMM absorber. (c) Real parts of the $\varepsilon_{\parallel}$ and $\varepsilon_{\perp}$ of the HMM absorber extracted from VASE as transiting the GST225 state from amorphous (top panel) to crystalline (bottom panel). (d) The VASE measured (top panel) and FDTD simulated (bottom panel) $A(\omega)$ of the HMM absorber for the amorphous and crystalline states.

$$\varepsilon_{\perp} = (\varepsilon_{Au} \times \varepsilon_{GST})/(f \times \varepsilon_{GST} + (1 - f) \times \varepsilon_{Au}) \quad (2)$$

where ε_{GST} and ε_{Au} are the permittivity of the GST225 and Au, respectively, $f = t_{Au}/(t_{Au} + t_{GST})$ the filling fraction, and t_{Au} and t_{GST} the thickness of the Au and the GST225 layer, respectively. The ε_{GST} values for both amorphous (ESI Fig. S1(a)†) and crystalline (ESI Fig. S1(b)†) states are measured using the VASE, respectively, which are fitted using the Tauc–Lorentz model. A Drude model is used to fit the measured ε_{Au} (ESI Fig. S1(c)†).[74] The top panel of Fig. 1(c) presents the measured real parts of $\varepsilon_{\perp}$ and $\varepsilon_{\parallel}$ of the HMM absorber for the as-deposited (AD) amorphous (AM) state. As is seen, the AD-AM HMM possesses the hyperbolic dispersions of type-I (real($\varepsilon_{\parallel}$) > 0, real($\varepsilon_{\perp}$) < 0) and type-II (real($\varepsilon_{\parallel}$) < 0, real($\varepsilon_{\perp}$) > 0) in the visible (λ < 700 nm) and N-IR (λ > 840 nm) regions, respectively. Afterwards, the HMM absorber is annealed at $T_g = 200$ °C in an argon atmosphere for 30 min. Such a temperature is above the crystallisation point of $T_c = 160$ °C but below the melting point of $T_m = 630$ °C,[61] which can change the structural state from amorphous to crystalline (CR). In the bottom panel, we show the real($\varepsilon_{\parallel}$) and real($\varepsilon_{\perp}$) of the annealed HMM absorber extracted from the VASE measurement. The type-II hyperbolic dispersion in the N-IR region is redshifted (λ > 1200 nm) by crystallising the absorber. The crystallised HMM absorber, however no longer exhibits type-I hyperbolic dispersion in the visible region. The large variation in ε_{GST} between the amorphous and crystalline structural phases (see ESI Fig. S1(a and b)†) engineers the optical transition matrix elements, that in turn, tunes the hyperbolic dispersion.

The reflectance ($R(\omega)$) and transmittance ($T(\omega)$) spectra of the HMM absorber are directly measured using VASE (see Methods for details). The absorptance is derived from $A(\omega) = 1 - R(\omega) - T(\omega)$. The absorber possesses a zero transmittance that can simplify the absorptance to $A(\omega) = 1 - R(\omega)$. In the top panel of Fig. 1(d), we first measure the $A(\omega)$ for both amorphous (blue solid line) and crystalline (red solid line) states. The chalcogenide HMM absorber possesses a nearly perfect absorptance in the N-IR region, with a peak absorptance of $A(\omega) = 0.99$ at the resonant wavelength of $\lambda_a = 1180$ nm for the amorphous phase. As transiting the structural state from amorphous to crystalline, peak $A(\omega)$ undergoes a radical redshift of 500 nm, while maintaining a high absorptance of $A(\omega) = 0.86$ at the resonant wavelength of $\lambda_c = 1680$ nm, permitting switching between two distinct spectra. Due to the widely spectral shift, our HMM absorber has a significant $A(\omega)$ contrast of $\Delta A(\omega) = 0.78$ at $\lambda_c = 1680$ nm. The numerically calculated HMM absorber $A(\omega)$ spectra agree with experimentally measured spectra. In the bottom panel, we have simulated the $A(\omega)$ spectra of the HMM absorber using the finite different time domain (FDTD) solver within Lumerical Solution.[75] The HMM absorber is simulated with normal plane wave illumination, and the wave vector points towards the $-z$ axis. The HMM geometry is set to those measured using the FIB cross-section image presented in Fig. 1(b). A detailed description of the numerical model can be found in the Method. The numerical calculation validates the spectral moving direction by changing the structural phase; it demonstrates that the theoretical $A(\omega)$ has a good agreement with the experimental $A(\omega)$. To simplify the numerical model, the surface roughness and fabrication defects are not considered. Such a simplification induces variations between the simulated and measured $A(\omega)$, as well as slight widening of the measured resonances. Moreover, the $A(\omega)$ spectra are measured in the far-field. However, in the model the $A(\omega)$ spectra are calculated in the near-field of the HMM absorber, which also causes variations between the calculation and measurement. The effective absorption for the light transmitting in the HMM absorber can be expressed as

$$\alpha_{\parallel,\perp}(\omega) = -\frac{\mathrm{Im}[\varepsilon_{\parallel,\perp}(\omega)]\omega}{\sqrt{\mathrm{Re}[|\varepsilon_{\parallel,\perp}(\omega)|]}} \quad (3)$$

where $\alpha_{\parallel}(\omega)$ and $\alpha_{\perp}(\omega)$ present effective absorption produced by beams transmitting along the z-axis and in the "x–y" plane, respectively.[76] Therefore, the absorption is dependent on the $\varepsilon_{\parallel,\perp}(\omega)$ having hyperbolic dispersion as shown in Fig. 1(c). To exploit the underlying mechanism of the tunable perfect absorption, it is instructive to study the effective impedance of the HMM absorber,[77,78]

$$Z_{HMM} = \frac{(T_{22} - T_{11}) \mp \sqrt{(T_{22} - T_{11})^2 + 4T_{12}T_{21}}}{2T_{21}} \quad (4)$$

where the transfer (T) matrix elements of T_{11}, T_{12}, T_{21}, and T_{22} can be expressed by

$$T_{11} = \frac{(1 + S_{11})(1 - S_{22}) + (S_{21}S_{12})}{2S_{21}} \quad (5)$$

$$T_{12} = \frac{(1+S_{11})(1+S_{22}) - (S_{21}S_{12})}{2S_{21}} \quad (6)$$

$$T_{21} = \frac{(1-S_{11})(1-S_{22}) - (S_{21}S_{12})}{2S_{21}} \quad (7)$$

$$T_{22} = \frac{(1-S_{11})(1+S_{22}) + (S_{21}S_{12})}{2S_{21}} \quad (8)$$

where the S_{11}, S_{12}, S_{21}, and S_{22} (scattering matrix (S) elements) are the scattering parameters of the reflectance and transmittance coefficient along the forward and backward directions, respectively. Moreover, according to Fresnel's equation, under a normal incidence, the reflectance of the HMM structure is defined as,[79]

$$R(\omega) = \left|\frac{Z_{HMM} - Z_{Air}}{Z_{HMM} + Z_{Air}}\right|^2 \quad (9)$$

where $Z_{Air} = 1$ is the impedance of free-space. A perfect absorptance can be achieved when the impedance of the HMM absorber (Z_{HMM}) matches the free space ($Z_{Air} = 1$). Fig. 2(a) shows the real part of the Z_{HMM} of the HMM absorber for the amorphous (blue solid line) and crystalline states (red solid line). For the amorphous state, the Z_{HMM} is nearly unity at the resonant wavelength of $\lambda_a = 1180$ nm, leading to the perfect absorptance ($A(\omega) = 0.99$). However, for the crystalline state the Z_{HMM} is decreased to 0.66 at the resonant wavelength of $\lambda_c = 1680$ nm that breaks the impedance match. Thus, a lower absorptance of $A(\omega) = 0.86$ occurs at $\lambda_c = 1680$ nm for the crystalline state. Fig. 2(b and c) show the FDTD simulated total electric (E-) field intensity and absorbed power (P_{abs}) distributions at $\lambda_a = 1180$ nm for the amorphous state and $\lambda_c = 1680$ nm for the crystalline state. In the pattern along the x–z plane, the white arrows represent the Poynting vector (S_p) whereas the color represents the magnitudes of the E-field intensity and power absorptance. The total E-field intensity distribution $|E|^2 = |E_x|^2 + |E_y|^2 + |E_z|^2$ relating to $A(\omega) = 0.99$ at $\lambda_a = 1180$ nm for the amorphous state is presented in the left column of Fig. 2(b). It clearly shows that the E-field can be well concentrated inside the HMM absorber while gradually attenuating along the z-direction. The power absorptance is expressed by $P_{abs} = 0.5\omega|E|^2\varepsilon_{im}$ and ε_{im} is the imaginary part of the permittivity.[80–82] As seen in the right column, the HMM can perfectly absorb the light although the P_{abs} gradually decays along the z-direction. Such a high absorptance is caused by the impedance match between the HMM and air for the amorphous state. In Fig. 2(c), we illustrate the E-field intensity (left column) and P_{abs} (right column) relating to $A(\omega) = 0.86$ at $\lambda_c = 1680$ nm for the crystalline state. It shows that the field patterns of the structure are very similar to the ones for the amorphous phase, which indicates that the HMM also possesses high absorptance after crystallising the GST225 films. The E-field intensity and P_{abs} in the HMM with amorphous GST225 (Fig. 2(b)) are stronger than for the crystalline phase (Fig. 2(c)), implying that a higher absorptance (better impedance match) can be achieved.

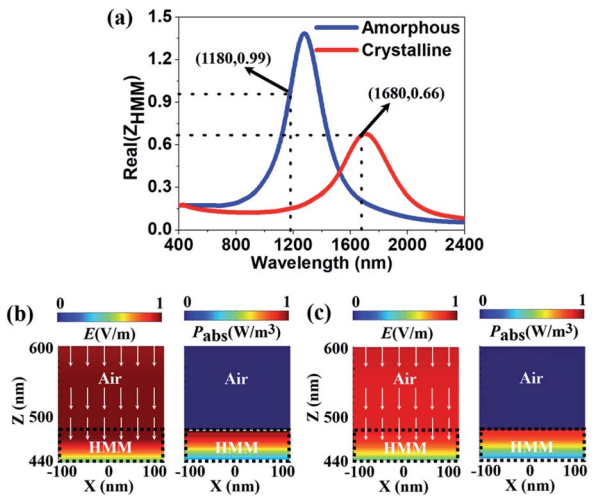

Fig. 2 (a) Effective impedance of the HMM absorber for both the amorphous (blue line) and crystalline (red line) states. (b and c) E-field intensity (left column) and absorbed power (right column) distributions of the HMM absorber for (b) the amorphous state at $\lambda_a = 1180$ nm, and (c) the crystalline state at $\lambda_c = 1680$ nm. The white arrows represent the Poynting vectors. The different regions of air and HMM are circled by the black dotted line.

The $A(\omega)$ spectra resonant wavelength can be tuned by varying the thickness of constituent layers. We fabricate a series of HMM absorbers with the thickness of the Au (T_{Au}) and GST225 (T_{GST}) layers changing from 20 to 40 nm, while fixing the filling factor at $f = 0.5$ (namely, $T_{Au} = T_{GST}$). In the top panel of Fig. 3(a), we experimentally illustrate the $A(\omega)$ of the amorphous HMM absorber for various thicknesses. As is observed, the resonant peak redshifts across the N-IR spectral range with increasing the thickness of constituent layers. Integrating this absorber into N-IR photonic devices can resolve a particular spectral band. Furthermore, those resonances can be switched by crystallising the GST225, as shown in the top panel of Fig. 3(b). The FDTD simulated $A(\omega)$ spectra match well the measured ones. The bottom panels of Fig. 3(a and b) show the comparison. A redshift in the resonant peak is observed by either increasing the layer thickness or crystallizing the GST225. In Fig. 3(c), we experimentally present how the resonant wavelength can be switched by combining both variations in the layer thickness and the structural phase of GST225. Such an ability to cover a large part of the N-IR spectrum by simply changing the thickness of constituent layers and crystallising the GST225 makes it essential to use a micrometer-size N-IR hyperspectral imaging camera. In Fig. 3(d), for the amorphous HMM absorber we have numerically demonstrated a 2D diagram of absorptance against T_{Au} and T_{GST} with a step of 0.5 nm at a fixed wavelength of $\lambda_a = 1180$ nm. As can be seen, the absorptance achieves the highest value of 0.99 at $\lambda_a = 1180$ nm for $T_{Au} = T_{GST} = 40$ nm.

Ideal thermal photovoltaics, photon detectors, and emitters are desired to absorb incident light perfectly under full incident angles regardless of polarisation. For our proposed HMM perfect absorber, the absorptance is also robust under oblique incident angles (θ_i) for both the p- and s-polarisations. Fig. 4 shows the measured (left column) and simulated (right column) $A(\omega)$ spectra as the θ_i increases from 20° to 80° in a 2° step,

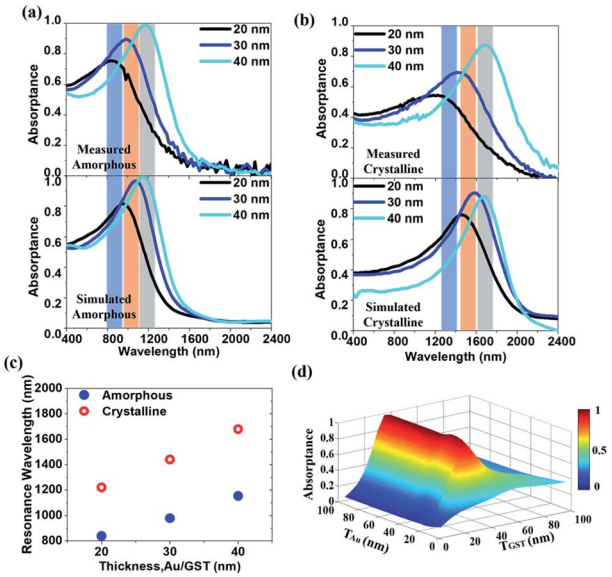

Fig. 3 (a and b) The performance of resonance switching in the HMM absorber: VASE measured (top panels) and FDTD simulated (bottom panels) absorptance spectra for the (a) amorphous and (b) crystalline states. The filling factor is $f = 0.5$ and the thickness of the constituent layer is $T_{Au} = T_{GST} = 20$ nm (black lines), 30 nm (blue lines), and 40 nm (cyan lines), respectively. The redshift of the absorptance spectra can be both experimentally and numerically found by changing the GST225 state from amorphous to crystalline. (c) The resonant wavelength is plotted against the thickness of constituent layers for both the amorphous (blue dot) and crystalline (red open circle) phases. (d) A 2D diagram of absorptance against T_{Au} and T_{GST} at a fixed wavelength of $\lambda_a = 1180$ nm.

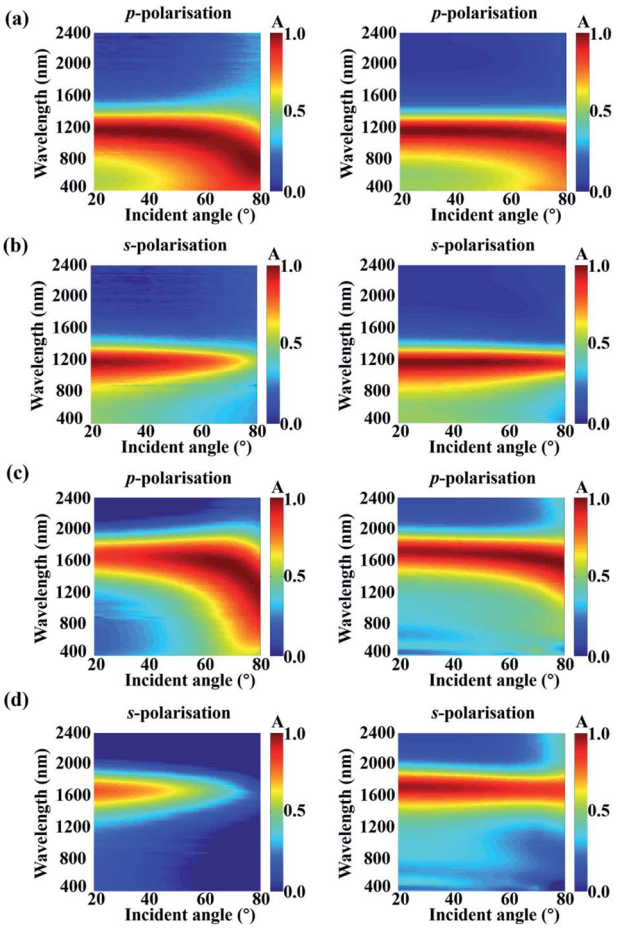

Fig. 4 The VASE measurement (left column) and FDTD simulation (right column) of incident angular-dependent absorptance spectra for the phase change HMM absorber on a SiO_2 substrate under the illumination of (a) p- and (b) s-polarized lights for the amorphous state and (c) p- and (d) s-polarized lights for the crystalline state.

where Fig. 4(a and b) present the $A(\omega)$ for the p- and s-polarisations in the amorphous state, respectively, Fig. 4(c and d) present the $A(\omega)$ for the p- and s-polarisations in the crystalline state, respectively. For the amorphous state, the $A(\omega)$ is maintained above 85% for $\theta_i < 50°$ from 1000 to 1250 nm under both p- and s-polarised incidences. Although the performance of the angular independent absorptance gets worse as transiting the GST structural state from amorphous to crystalline, there is a good spectral overlap between the $A(\omega)$ for p- and s-polarisations in each structural state. Therefore, the $A(\omega)$ of the HMM is not only omnidirectional but polarisation independent. There is a difference between the measured and simulated absorptance. This may stem from scattering of radiation from imperfections of fabrication.[83] In the numerical model, a few factors are not considered, for example, the thickness of the native oxide layer, uncertainty in the incident angle, imperfections of fabrication, surface roughness, and grain boundaries. Such a simplification induces the observed discrepancy between the simulated and measured reflectance spectra. Meanwhile, the error in layer thickness monitoring in the deposition process may also cause the difference. Moreover, the reflectance was measured in the far-field *via* a focusing probe with ~0.01 NA. Yet, in the model, the reflectance was recorded by the power monitor positioned above the HMM absorber, causing the differences between the experiment and simulation.

The GST225 film can be reliably switched more than 10^8 cycles between the amorphous and crystalline phases,[84,85] which is a key advantage for reconfigurable photonic devices. This can enable various functionalities in the same photonic structure without changing its geometry. In this work, the reversible transition between the amorphous and crystalline phases results in a huge alteration in the complex permittivity $\varepsilon_{GST} =$ real(ε_{GST}) + imag(ε_{GST}) $\times$ i (see ESI Fig. S1†), leading to a reversible tuning of the resonant frequency of peak absorptance. In ESI Fig. S2,† we schematically illustrate the treatment of the phase change HMM absorber. First, the as-deposited amorphous (AD-AM) HMM absorber is crystallised by thermally heating the structure for 30 min at $T_g = 200$ °C on a Linkam hotplate in a flowing argon atmosphere. To reversibly change the GST225 state from crystalline (CR) to melt quenched amorphous (MQ-AM), the crystal lattice has to be melt and quenched promptly at a rate of 10^9 to 10^{10} K s^{-1} to freeze the Ge, Sb, and Te atoms in the random position to form the disorder MQ-AM state.[86] A single 5 nanosecond (ns) laser pulse can produce the sufficient energy to increase the local temperature momentarily above $T_m = 630$ °C to melt the GST225. The

subsequent prompt cooling quenches the melted layer into the AM phase. Finally, to recrystallise (R-CR) the HMM with the MQ-AM GST225, the hot plate is employed to maintain the HMM above $T_c = 160$ °C but below $T_m = 630$ °C. A phase transition cycle of crystallisation (AD-AM → CR), reamorphisation (CR → MQ-AM), and recrystallisation (MQ-AM → R-CR) takes place at different temperatures and time scales. The reversible optical switching (namely, an amorphisation of GST225) is experimentally triggered by irradiating the sample with ns laser pulses.[87]

As schematically shown in Fig. 5(a), a home-built laser system consisting of a Q-switch pulsed laser (Quintel, Q-smart 850) operating at $\lambda = 1064$ nm, 5 ns pulse duration with a 10 Hz repetition rate is employed to amorphise the HMM absorber. The maximum output energy of the laser pulse is 850 mJ with a circular beam radius of 5 mm. To optimise the switching energy, a few laser amorphised marks (grey area circled by the white dashed line) are fabricated on the sample surface by using different laser energies. These marks are made on various areas by moving the sample *via* the translation stage. Fig. 5(b) shows the measured $A(\omega)$ spectra at the different marks. Initially, the HMM absorber with crystalline GST225 has a peak absorptance of $A(\omega) = 0.86$ at $\lambda_c = 1680$ nm (red line). As increasing the laser energy from 0 mJ to 34.3 mJ, the $A(\omega)$ spectrum does not significantly change, indicating that the HMM structure is not yet amorphised. By increasing the energy to 40.8 mJ, the resonant peak massively blue shifts to $\lambda_m =$ 1280 nm. However for the energy above 40.8 mJ, the resonant wavelength no longer shifts while the ablation effect slightly reduces the peak absorptance.[88,89] Thus, the laser switching energy of 40.8 mJ is employed to amorphise the HMM absorber. In Fig. 5(c–f), we present experimentally a phase change HMM absorber operating in the N-IR region using a reversible phase transition of GST225 between the amorphous and crystalline states. The $A(\omega)$ spectra of the HMM absorber measured at the four structural states of AD-AM (blue line), hot plate annealed CR (red line), ns laser-induced MQ-AM (orange line), and hot plate annealed R-CR (cyan line) are presented, respectively. The resonant wavelength of the HMM absorber can redshift from $\lambda_a = 1180$ to $\lambda_c = 1680$ nm as transiting the structural state from AD-AM (Fig. 5(c)) to CR (Fig. 5(d)). The CR-HMM is subsequently reamorphised to the MQ-AM state (Fig. 5(e)), leading to a blue-shift of the resonant wavelength from $\lambda_c = 1680$ nm to $\lambda_{MQ} = 1280$ nm. The MQ-AM HMM can be fully recrystallised to move the resonant wavelength from $\lambda_{MQ} = 1280$ nm to $\lambda_{RC} = 1680$ nm (Fig. 5(f)). The insets show the microscopy images of the HMM absorber at the various states, accordingly. The CR-HMM appears (Fig. 5(d)) to be brighter than AM-HMM (Fig. 5(c)) due to a decreasing absorptance after crystallisation. The MQ-AM HMM can change back to a dark color (circled by a dotted line in Fig. 5(e)), indicating an increasing absorptance. The restored, recrystallized HMM (Fig. 5(f)) has a similar color to that crystallised in the first writing. Although the resonant wavelength of the CR-HMM ($\lambda_c = 1680$ nm) perfectly matches that of the R-CR HMM ($\lambda_{RC} = 1680$ nm), a difference occurs in the resonant wavelengths between the AD-AM ($\lambda_a = 1180$ nm) and MQ-AM ($\lambda_{MQ} = 1280$ nm) states. It is because that the optical and structural properties of the as-deposited (AD) amorphous (AM) phase are slightly different than those of the melt-quenched (MQ) amorphous (AM) state. A detailed comparison can be found in the ESI of ref. 90. The laser induced amorphization (MQ-AM) is not sufficient to cause a complete reversion to the AD-AM state, and there are different crystallisation kinetics between the AD-AM and MQ-AM structural states.[88,91,92] Indeed, the MQ-AM state is intermediate in structure between the AD-AM and CR phases. As seen in Fig. 5(c–e), the absorptance spectrum of HMM for the MQ-AM state is located between the spectra of the AD-AM and CR samples. The reconfigurable absorptance control and dynamic band-selectivity in the HMM absorber offer a main advantage over the previous light absorber, not to mention its potential to convert the absorbed light energy into electron–hole pairs. In ESI Fig. S3,† we numerically studied the effect of the layer period (P) on the absorptance using Lumerical solution. We find that the peak absorptance for the HMM absorber with the amorphous state becomes higher as increasing P from 4 to 6 while maintaining the peak value around 1182 nm when $P > 6$. This indicates that layers of period of 6 ($P = 6$) can be seen as an effective material.

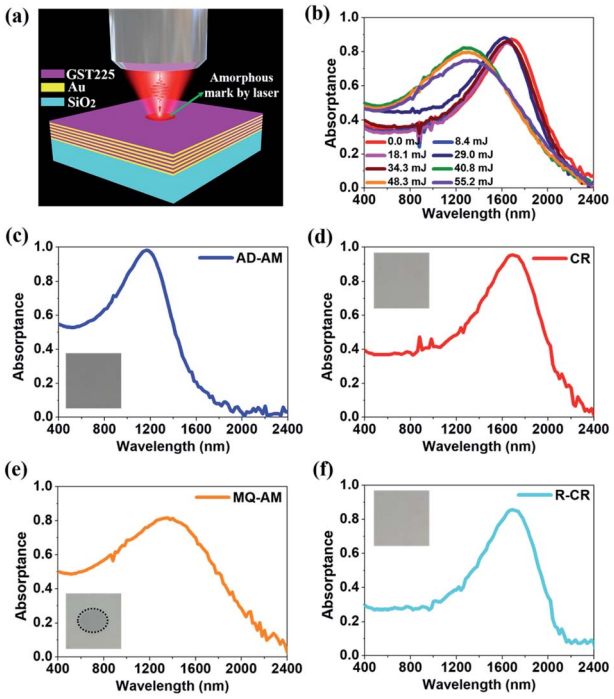

Fig. 5 (a) Schematic illustration of the laser amorphised mark on the CR-HMM. (b) Absorptance spectra of the CR-HMM under the various laser energies of 0, 8.4, 18.1, 29.0, 34.3, 40.8, 48.3, and 55.2 mJ. (c–f) The absorptance spectra of the phase change HMM absorber with the different phases of (c) AD-AM, (d) CR, (e) MQ-AM, and (f) R-CR, where the insets are the microscope images of the HMM absorber.

3. Conclusions

In conclusion, we both experimentally and theoretically demonstrate a versatile platform for achieving reconfigurable,

polarisation-independent, and omnidirectional near-perfect light absorption across the N-IR region. The exceptional performance of the absorber is achieved by using a hyperbolic metamaterial based on the multi-layered Au–GST225 nanocomposite system. We show that the effective permittivity of the structure can be switched by changing the GST225 phases, leading to a large and reversible tuning in the peak absorption wavelength of 500 nm. Such a large-size absorber is efficient over the N-IR regime and can be straightforwardly fabricated without using high-resolution lithography and high-temperature growth methods. This shows its main advantages over nanostructured light absorbers. We anticipate that such a lithography-free technique is widespread and can be applied to other low-cost metal films *i.e.*, aluminum (Al). Not only would it offer excellent new scalable and high-throughput approaches, but also provide a monolithic integration into CMOS electronics. Such a phase change hyperbolic absorber has a promising impact in the areas of solar thermophotovoltaics, optical filtering, sensing technologies and thermal camouflage techniques.

4. Methods

4.1 Device fabrication

The HMM structure is fabricated by using the physical vapour deposition method. The sputter chamber base pressure is less than 6.0×10^{8} mTorr and all the deposition is carried out at 3.0 mTorr. The GST225 films were deposited by radio frequency (RF) sputtering with a power of 20 W and deposition rate of 2 Å s^{-1}. The Au films are deposited by direct current (DC) sputtering from an Au target (50 W, deposition rate of 2 Å s^{-1}). Thick samples (>200 nm) of both the materials were deposited, and the deposition rates were calibrated using an Atomic Force Microscope (AFM). Apart from the HMM structure, individual GST and Au films were deposited for the optical spectroscopic and crystallisation temperature measurements. All the samples are deposited onto the silica substrate and the as-deposited samples are in the amorphous state. The cross-sectional analysis and the corresponding elemental analysis of the layered planner HMM structure are performed using a focused ion beam (Helios G4 UX) system.

4.2 Optical characterisation

The optical characterisation of the HMM absorber is performed using variable angle spectroscopic ellipsometry (J. A. Woollam Co., Inc, V-VASE). The optical permittivity of the structure is measured in the wavelength range of 400–2400 nm with a spectroscopic resolution of 10 nm. The polarisation and the angle-dependent transmittance and reflectance of the HMM structures are measured with the incident angle varying from 20° to 80° at room temperature. The reflectance and transmittance spectra are recorded at an angular resolution of 5°. The reconfigurability response of the HMM structure was measured by a laser switching experiment. A home-built laser system consisting of a ns pulsed laser operating at 1064 nm, 10 ns pulse duration with a 30 Hz repetition rate was employed to switch the HMM devices.

4.3 Numerical simulation

A commercial FDTD simulation software package (Lumerical Solutions, version 8.15.736) was used to simulate the HMM absorber. The simulation for the planar HMM structure is performed in a 3D layout, and a unit cell of 200 nm × 200 nm × 3500 nm in the *x*–*y*–*z* plane is considered for the simulation. In the model, periodic boundary conditions in the *x*–*y* plane and perfectly matched layers along the wave propagation direction (*z*-axis) are used. The reflectance and the transmittance spectra are recorded by the power monitors placed above and below the HMM absorber, respectively. The Bloch boundary condition was used for normal incidence whilst a broadband fixed angle source technique (BFAST) was used for oblique incidence. The spatial grid size of 2 nm was used to minimise the simulation error. The complex permittivity of Au and GST225 with the different states is obtained by ellipsometry (see ESI Fig. S1†).

Author contributions

T. C. conceived the idea and supervised the work. K. L. designed the device. J. B. fabricated and measured the device. M. L. performed the analysis of data. The manuscript was written through contributions of all authors. All authors have given approval to the final version of the manuscript. T. C. and J. B. contributed equally to this work.

Conflicts of interest

There are no conflicts to declare.

Acknowledgements

The work presented herein was supported by the National Key Research and Development Program of China with grant number 2019YFA0709100 and LiaoNing Revitalization Talents Program with grant number XLYC1807237.

References

1 P. N. Dyachenko, S. Molesky, A. Y. Petrov, M. Stormer, T. Krekeler, S. Lang, M. Ritter, Z. Jacob and M. Eich, *Nat. Commun.*, 2016, **7**, 11809.
2 N. L. Mou, X. L. Liu, T. Wei, H. X. Dong, Q. He, L. Zhou, Y. Q. Zhang, L. Zhang and S. L. Sun, *Nanoscale*, 2020, **12**, 5374–5379.
3 H. Yuan, X. Liu, F. Afshinmanesh, W. Li, G. Xu, J. Sun, B. Lian, A. G. Curto, G. J. Ye and Y. Hikita, *Nat. Nanotechnol.*, 2015, **10**, 707–713.
4 L. Zhou, Y. Tan, D. Ji, B. Zhu, P. Zhang, J. Xu, Q. Gan, Z. Yu and J. Zhu, *Sci. Adv.*, 2016, **2**, e1501227.
5 S. Wang, B. D. Weil, Y. Li, K. X. Wang, E. C. Garnett, S. Fan and Y. Cui, *Nano Lett.*, 2013, **13**, 4393–4398.
6 M. D. Kelzenberg, S. W. Boettcher, J. Petykiewicz, D. B. Turnerevans, M. C. Putnam, E. L. Warren, J. M. Spurgeon, R. M. Briggs, N. S. Lewis and H. A. Atwater, *Nat. Mater.*, 2010, **9**, 239–244.

7 T. Cao, C. Wei, R. E. Simpson, L. Zhang and M. J. Cryan, *Sci. Rep.*, 2015, **4**, 3955.
8 B.-X. Wang, Y. He, P. Lou and W. Xing, *Nanoscale Adv.*, 2020, **2**, 763–769.
9 K. X. Wang, Z. Yu, V. Liu, Y. Cui and S. Fan, *Nano Lett.*, 2012, **12**, 1616–1619.
10 Q. Lin, L. Lu, M. M. Tavakoli, C. Zhang, G. C. Lui, Z. Chen, X. Chen, L. Tang, D. Zhang and Y. Lin, *Nano Energy*, 2016, 539–547.
11 T. Cao, L. Zhang, R. E. Simpson and M. J. Cryan, *J. Opt. Soc. Am. B*, 2013, **30**, 1580–1585.
12 C. K. Borah, P. K. Tyagi and S. Kumar, *Nanoscale Adv.*, 2020, **2**, 3231–3243.
13 T. Cao, K. Liu, L. Lu, H. C. Chui and R. E. Simpson, *Nanoscale*, 2019, **11**, 20546–20553.
14 Z. Liu, X. Liu, S. Huang, P. Pan, J. Chen, G. Liu and G. Gu, *ACS Appl. Mater. Interfaces*, 2015, **7**, 4962–4968.
15 B. Xiong, L. Deng, R. Peng and Y. Liu, *Nanoscale Adv.*, 2019, **1**, 3786–3806.
16 A. Tittl, A. U. Michel, M. Schaferling, X. Yin, B. Gholipour, L. Cui, M. Wuttig, T. Taubner, F. Neubrech and H. Giessen, *Adv. Mater.*, 2015, **27**, 4597–4603.
17 M. Seo, H. Lee, H. Kim and M. Lee, *Nanoscale Adv.*, 2019, **1**, 4090–4098.
18 W. Dong, H. Liu, J. K. Behera, L. Lu, R. J. H. Ng, K. V. Sreekanth, X. Zhou, J. K. W. Yang and R. E. Simpson, *Adv. Funct. Mater.*, 2019, **29**, 1806181.
19 N. C. D. Nath, S. Y. Choi, H. W. Jeong, J. Lee and H. Park, *Nano Energy*, 2016, **25**, 51–59.
20 J. Liang, L. Hou and J. Li, *J. Opt. Soc. Am. B*, 2016, **33**, 1075–1080.
21 S. S. Mirshafieyan and D. A. Gregory, *Sci. Rep.*, 2018, **8**, 2635.
22 Y. Fan, Z. Liu, F. Zhang, Q. Zhao, Z. Wei, Q. Fu, J. Li, C. Gu and H. Li, *Sci. Rep.*, 2015, **5**, 13956.
23 H. R. Seren, G. R. Keiser, L. Cao, J. Zhang, A. C. Strikwerda, K. Fan, G. D. Metcalfe, M. Wraback, X. Zhang and R. D. Averitt, *Adv. Opt. Mater.*, 2014, **2**, 1221–1226.
24 M. Faraji, M. K. Moravvejfarshi and L. Yousefi, *Opt. Commun.*, 2015, **355**, 352–355.
25 N. I. Landy, S. Sajuyigbe, J. J. Mock, D. R. Smith and W. J. Padilla, *Phys. Rev. Lett.*, 2008, **100**, 207402.
26 P. Chevalier, P. Bouchon, J. Jaeck, D. Lauwick, N. Bardou, A. Kattnig, F. Pardo and R. Haidar, *Appl. Phys. Lett.*, 2015, **107**, 251108.
27 D. Choi, C. K. Shin, D. Yoon, D. S. Chung, Y. W. Jin and L. P. Lee, *Nano Lett.*, 2014, **14**, 3374–3381.
28 D. Chanda, K. Shigeta, T. Truong, E. Lui, A. Mihi, M. V. Schulmerich, P. V. Braun, R. Bhargava and J. A. Rogers, *Nat. Commun.*, 2011, **2**, 479.
29 X. Luo, *Handbook of Laser Micro- and Nano-Engineering*, 2020, pp. 1–40.
30 M. Pu, Y. Guo, X. Li, X. Ma and X. Luo, *ACS Photonics*, 2018, **5**, 3198–3204.
31 X. Luo, *Sci. China: Phys., Mech. Astron.*, 2015, **58**, 594201.
32 D. R. Smith and D. Schurig, *Phys. Rev. Lett.*, 2012, **90**, 077405.
33 G. Yu, N. Ward, C. L. Cortes and J. Zubin, *Adv. OptoElectron.*, 2012, **2012**, 1–9.
34 Z. Jacob, I. I. Smolyaninov and E. E. Narimanov, *Appl. Phys. Lett.*, 2012, **100**, 181105.
35 Z. Liu, H. Lee, Y. Xiong, C. Sun and X. Zhang, *Science*, 2007, **315**, 1686.
36 B. Wang, Z. Liu, L. Zhou, Y. Fei, C. Yang, L. Mi, Q. Mu and J. Ma, *Nanoscale*, 2020, **12**, 16864–16874.
37 V. Caligiuri, L. Pezzi, A. Veltri and A. De Luca, *ACS Nano*, 2017, **11**, 1012–1025.
38 C. Pfeiffer and A. Grbic, *Phys. Rev. Lett.*, 2013, **110**, 197401.
39 T. Zhang, M. Wang, Y. Yang, F. Fan, T. Lee, H. Liu and D. Xiang, *Nanoscale*, 2018, **10**, 5097–5104.
40 K. V. Sreekanth, K. H. Krishna, A. De Luca and G. Strangi, *Sci. Rep.*, 2015, **4**, 6340.
41 K. V. Sreekanth and R. E. Simpson, *Opt. Commun.*, 2019, **440**, 150–154.
42 A. Kabashin, P. R. Evans, S. Pastkovsky, W. Hendren, G. A. Wurtz, R. Atkinson, R. Pollard, V. A. Podolskiy and A. V. Zayats, *Nat. Mater.*, 2009, **8**, 867–871.
43 X. Li, X. Ding, Y. Li, L. Wang and J. Fan, *Nanoscale*, 2016, **8**, 9852–9860.
44 A. J. Hoffman, L. Alekseyev, S. S. Howard, K. J. Franz, D. Wasserman, V. A. Podolskiy, E. E. Narimanov, D. L. Sivco and C. F. Gmachl, *Nat. Mater.*, 2007, **6**, 946–950.
45 K. Halterman and J. M. Elson, *Opt. Express*, 2014, **22**, 7337–7348.
46 P. Shekhar, J. Atkinson and Z. Jacob, *Nano Convergence*, 2014, **1**, 14.
47 K. V. Sreekanth, M. Elkabbash, Y. Alapan, A. R. Rashed, U. A. Gurkan and G. Strangi, *Sci. Rep.*, 2016, **6**, 26272.
48 Y. Cui, K. H. Fung, J. Xu, H. Ma, Y. Jin, S. He and N. X. Fang, *Nano Lett.*, 2012, **12**, 1443–1447.
49 H. Lin, B. C. P. Sturmberg, K. T. Lin, Y. Yang, X. Zheng, T. K. Chong, C. M. De Sterke and B. Jia, *Nat. Photonics*, 2019, **13**, 1–7.
50 M. Desouky, A. M. Mahmoud and M. A. Swillam, *Sci. Rep.*, 2018, **8**, 2036.
51 G. T. Papadakis and H. A. Atwater, *Phys. Rev. B: Condens. Matter Mater. Phys.*, 2015, **92**, 184101.
52 Z. Cao, X. Xiang, C. Yang, Y. Zhang, Z. Peng and L. Xuan, *Liq. Cryst.*, 2016, **43**, 1753–1759.
53 W. Li, Z. Liu, X. Zhang and X. Jiang, *Appl. Phys. Lett.*, 2012, **100**, 161108.
54 S. Prayakarao, B. Mendoza, A. Devine, C. Kyaw, R. B. Van Dover, V. Liberman and M. A. Noginov, *Appl. Phys. Lett.*, 2016, **109**, 061105.
55 Z. L. Samson, K. F. Macdonald, F. De Angelis, B. Gholipour, K. Knight, C. Huang, E. D. Fabrizio, D. W. Hewak and N. I. Zheludev, *Appl. Phys. Lett.*, 2010, **96**, 143105.
56 T. Cao, X. Zhang, W. Dong, L. Lu, X. Zhou, X. Zhuang, J. Deng, X. Cheng, G. Li and R. E. Simpson, *Adv. Opt. Mater.*, 2018, **6**, 1800169.
57 D. Shrekenhamer, W. Chen and W. J. Padilla, *Phys. Rev. Lett.*, 2013, **110**, 177403.
58 M. Wuttig, H. Bhaskaran and T. Taubner, *Nat. Photonics*, 2017, **11**, 465–476.
59 P. Li, X. Yang, T. W. W. Mas, J. Hanss, M. Lewin, A. U. Michel, M. Wuttig and T. Taubner, *Nat. Mater.*, 2016, **15**, 870–875.

60 T. Cao, L. Tian, H. Liang and K. Qin, *Microsyst. Nanoeng.*, 2018, **4**, 7.
61 T. Cao, L. Fang, Y. Cao, N. Li, Z. Fan and Z. Tao, *Sci. Bull.*, 2019, **64**, 814–822.
62 T. Cao, R. E. Simpson and M. J. Cryan, *J. Opt. Soc. Am. B*, 2013, **30**, 439–444.
63 Q. Wang, E. T. F. Rogers, B. Gholipour, C. Wang, G. Yuan, J. Teng and N. I. Zheludev, *Nat. Photonics*, 2016, **10**, 60–65.
64 T. Cao, G. Zheng, S. Wang and C. Wei, *Opt. Express*, 2015, **23**, 18029–18039.
65 C. R. De Galarreta, A. M. Alexeev, Y. Au, M. Lopezgarcia, M. Klemm, M. J. Cryan, J. Bertolotti and C. D. Wright, *Adv. Funct. Mater.*, 2018, **28**, 1704993.
66 T. Cao, L. Zhang, R. E. Simpson, C. Wei and M. J. Cryan, *Opt. Express*, 2013, **21**, 27841–27851.
67 X. Yin, M. Schaferling, A. U. Michel, A. Tittl, M. Wuttig, T. Taubner and H. Giessen, *Nano Lett.*, 2015, **15**, 4255–4260.
68 G. P. Agrawal, *Fiber-Optic Communication Systems*, 4th edn, 2011.
69 K. V. Shportko, S. Kremers, M. Woda, D. Lencer, J. Robertson and M. Wuttig, *Nat. Mater.*, 2008, **7**, 653–658.
70 A. Poddubny, I. Iorsh, P. Belov and Y. Kivshar, *Nat. Photonics*, 2013, **7**, 948–957.
71 L. Lu, R. E. Simpson and S. K. Valiyaveedu, *J. Opt.*, 2018, **20**, 103001.
72 B. Wood, J. B. Pendry and D. P. Tsai, *Phys. Rev. B: Condens. Matter Mater. Phys.*, 2006, **74**, 115116.
73 J. Schilling, *Phys. Rev. E: Stat., Nonlinear, Soft Matter Phys.*, 2006, **74**, 046618.
74 P. B. Johnson and R. W. Christy, *Phys. Rev. B: Solid State*, 1972, **6**, 4370–4379.
75 FDTD Solutions, http://www.lumerical.com.
76 B. Janaszek, A. Tyszka-Zawadzka and P. Szczepański, *Opt. Express*, 2017, **25**, 13153–13162.
77 D. R. Smith, D. C. Vier, T. Koschny and C. M. Soukoulis, *Phys. Rev. E: Stat., Nonlinear, Soft Matter Phys.*, 2005, **71**, 036617.
78 Z. Szabo, G. Park, R. Hedge and E. Li, *IEEE Trans. Microwave Theory Tech.*, 2010, **58**, 2646–2653.
79 L. Feng, P. Huo, Y. Liang and T. Xu, *Adv. Mater.*, 2019, 1903787.
80 X. Chen, Y. Chen, M. Yan and M. Qiu, *ACS Nano*, 2012, **6**, 2550–2557.
81 B. Zhao and Z. M. Zhang, *Nanoscale Microscale Thermophys. Eng.*, 2017, **21**, 123–133.
82 L. Wen, Y. Chen, L. Liang and Q. Chen, *ACS Photonics*, 2018, **5**, 581–591.
83 H. Tao, C. Bingham, A. Strikwerda, D. Pilon, D. Shrekenhamer, N. Landy, K. Fan, X. Zhang, W. Padilla and R. Averitt, *Phys. Rev. B: Condens. Matter Mater. Phys.*, 2008, **78**, 241103.
84 M. Wuttig and N. Yamada, *Nat. Mater.*, 2007, **6**, 824–832.
85 M. Terao, T. Morikawa and T. Ohta, *Jpn. J. Appl. Phys.*, 2009, **48**, 080001.
86 V. Weidenhof, N. Pirch, I. Friedrich, S. Ziegler and M. Wuttig, *J. Appl. Phys.*, 2000, **88**, 657–664.
87 J. Orava, A. L. Greer, B. Gholipour, D. W. Hewak and C. E. Smith, *Nat. Mater.*, 2012, **11**, 279–283.
88 S. Raoux, R. Shelby, B. Munoz, M. Hitzbleck, D. Krebs, M. Salinga, M. Woda, M. Austgen, K.-M. Chung and M. Wuttig, *Presented in Part at the Eur Phase Change Ovonic Science Symposium*, 2008.
89 R. E. Simpson, P. Fons, X. L. Wang, A. V. Kolobov, T. Fukaya and J. Tominaga, *Appl. Phys. Lett.*, 2010, **97**, 161906.
90 L. Waldecker, T. A. Miller, M. Rudé, R. Bertoni, J. Osmond, V. Pruneri, R. E. Simpson, R. Ernstorfer and S. Wall, *Nat. Mater.*, 2015, **14**, 991–995.
91 J. K. Behera, X. Zhou, J. Tominaga and R. E. Simpson, *Opt. Mater. Express*, 2017, **7**, 3741–3759.
92 M. Salinga, E. Carria, A. Kaldenbach, M. Bornhofft, J. Benke, J. Mayer and M. Wuttig, *Nat. Commun.*, 2013, **4**, 2371.